

Paleoceanography and Paleoclimatology



RESEARCH ARTICLE

10.1029/2018PA003458

Key Points:

- Mediterranean Sea sediments record multicentennial variability in productivity and anoxia (Ba/Ti, Br/Ti, and Mo/Ti) during sapropel S5
- We corrected our time series for changes in sedimentation rate on a multicentennial time scale, by using “spectral simplicity”
- Sedimentation covaries with monsoon variability during S5, while multicentennial variability may be linked to solar variability

Supporting Information:

- Supporting Information S1
- Data Set S1

Correspondence to:

J. P. Dirksen,
j.p.dirksen@uu.nl

Citation:

Dirksen, J. P., Hennekam, R., Geerken, E., & Reichart, G.-J. (2019). A novel approach using time-depth distortions to assess multicentennial variability in deep-sea oxygen deficiency in the Eastern Mediterranean Sea during sapropel S5. *Paleoceanography and Paleoclimatology*, 34, 774–786. <https://doi.org/10.1029/2018PA003458>

Received 8 AUG 2018

Accepted 6 FEB 2019

Accepted article online 16 APR 2019

Published online 13 MAY 2019

©2019. The Authors.

This is an open access article under the terms of the Creative Commons AttributionNonCommercialNoDerivs License, which permits use and distribution in any medium, provided the original work is properly cited, the use is noncommercial and no modifications or adaptations are made.

A Novel Approach Using Time-Depth Distortions to Assess Multicentennial Variability in Deep-Sea Oxygen Deficiency in the Eastern Mediterranean Sea During Sapropel S5

Jan Pieter Dirksen¹ , Rick Hennekam² , Esmee Geerken², and Gert-Jan Reichart^{1,2}

¹Department of Earth Sciences, Faculty of Geosciences, Utrecht University, Utrecht, The Netherlands, ²NIOZ Royal Netherlands Institute for Sea Research, Department of Ocean Systems, and Utrecht University, Texel, The Netherlands

Abstract Reconstructing millennial- to centennial-scale climate variability for the Eemian—an interval with estimated sea surface temperatures ~ 0.5 °C warmer than “preindustrial”—requires records with high temporal resolution. Sapropel S5 sediments, deposited under anoxic conditions in the Eastern Mediterranean Sea, offer the rare opportunity to assess multicentennial climate variability during this time. Here we present high-resolution S5 piston core data from the Nile delta region. Specifically, we focus on Ba/Ti, Br/Ti, and Mo/Ti, as they are proxies for paleo-productivity, marine organic carbon, and sediment anoxia, respectively. A high correlation between our Ba/Ti values in core 64PE-406-E1 and well-dated Ba records of nearby cores (LC21 and ODP967) was found. We, therefore, tuned our data to these cores obtaining an initial age model. A time-frequency analyses indicated significant frequency content in the multicentennial band, although the frequency components drifted over time. Assuming spectral simplicity, we corrected for sedimentation rate changes on a multicentennial time scale. This novel approach grants a higher-resolution age model. The resulting variability in sedimentation rate is similar to records of monsoon variability, indicating a possible link between sedimentation at the core location and low-latitude monsoon variability, linked via the River Nile. Moreover, the periodicities found in the sapropel time series are similar to the frequency content of total solar irradiance and sunspot records known for the Holocene, at least at high frequencies (~ 50 – 150 years). Hence, our data suggest cyclic intrasapropel variability, at least during the deposition of sapropel S5, may be linked to solar cycles.

1. Introduction

During the Quaternary period, climate has fluctuated between glacial and interglacial states, paced by astronomically driven changes in insolation, on time scales of 10^4 to 10^5 years (e.g., Tzedakis et al., 2017). Millennial-scale oscillations were first identified by Heinrich (1988), who found periodically occurring ice rafted detritus in the North Atlantic. Later, climate oscillations on time scales of 10^2 to 10^3 years were first recognized in the ice cores from Greenland (Dansgaard et al., 1993) and by Grootes et al. (1993) in the same year. At the same time, it was reported that during the last interglacial (Eemian), climate was more unstable than during the present interglacial, at least in Greenland (GRIP Members, 1993, and later also NEEM community members, 2013), and suborbital climate variability during this time interval was later also shown in Atlantic sediment records (Oppo et al., 2001, 2006). The discovery of the high-frequency climate oscillations resulted in a quest for similar frequency changes in other records, in both the continental (Blaga et al., 2013; Wang et al., 2001) and the marine realm (Altabet et al., 2002; Haug et al., 2001). Some studies suggest that these high-frequency climate oscillations are linked to glacial conditions or that the glacial boundary conditions at least enhance the impact of some unknown inherent oscillation of the climate system (e.g., Bond et al., 1993, 1997), although they have also been found in nonglacial conditions (for example, Barker et al., 2011). We further investigate this suborbital climate variability in a relatively warm climate. These results can therefore also be used to assess the importance of multicentennial climate variability for near future climate change.

Of particular interest is Marine Isotope Stage 5e (MIS-5e; ~ 129 – 116 ka), where global sea surface temperatures may have been $\sim 0.5^\circ$ warmer than preindustrial levels (Hoffman et al., 2017). MIS-5e may not be a perfect analogue for future global warming, as anthropogenic forcing differs significantly from natural forcing

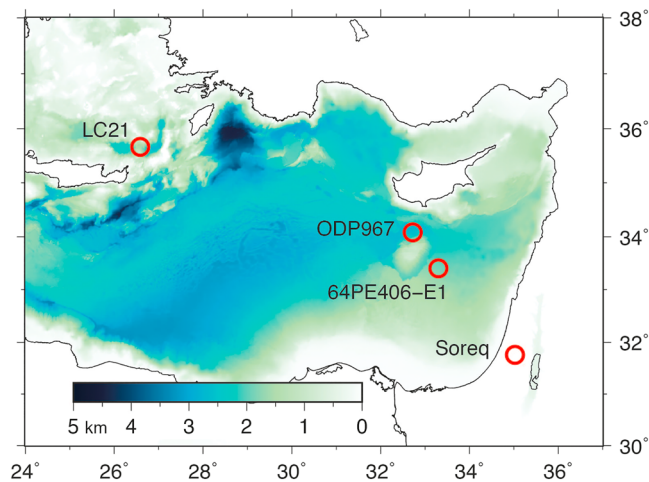


Figure 1. Bathymetric map of the Eastern Mediterranean Sea, indicating the locations of cores 64PE406-E1 (this study), LC21, and ODP967, as well as the location of Soreq cave.

(and due to the different orbital parameters), but still this interval can give valuable information on mechanisms and feedbacks that operate in a comparable warmer climate (e.g., Capron et al., 2017). Although this time interval has been studied extensively, very few studies achieved a sufficient resolution to investigate multicentennial climate variability. Most continental records lack sufficient time control, whereas marine records mostly lack resolution due to bioturbation.

The Mediterranean Sea is one of the few basins that allow studying high-resolution climate change at the lower latitudes during warm intervals. Limited water exchange with the open ocean makes the Mediterranean Sea, with its antiestuarine overturning circulation, extremely vulnerable to climatic perturbations. This is exemplified by the repeated deposition of organic-rich layers in the Eastern Mediterranean Sea, that is, sapropels, linked to precession minima (Cramp & O'Sullivan, 1999; Hilgen, 1991; Lourens et al., 1996; Rohling et al., 2015; Rossignol-Strick, 1985; Rossignol-Strick et al., 1982). Sapropels are thought to reflect changes in the Northeast African monsoon intensity, which affect mainly Nile outflow (Rohling et al., 2015; Rossignol-Strick, 1985), reducing deep sea ventilation. Concomitantly increasing eastern Mediterranean productiv-

ity due to the development of a deep chlorophyll maximum, additional nutrients from the Nile River, and/or phosphorus regeneration from anoxic sediments, as well as related remineralization at depth, is suggested to result in bottom water anoxia and enhanced preservation of organic matter (De Lange et al., 2008; Kemp et al., 1999; Krom et al., 2002; Rohling & Gieskes, 1989; Rohling et al., 2015; Slomp et al., 2002; van Santvoort et al., 1996, 1997). The lack of bioturbation during these anoxic periods produces perfectly preserved sedimentary archives, allowing high-resolution climate reconstructions.

Sapropel deposition is thought to occur time-synchronous (within age uncertainties) in the entire Mediterranean Sea basin, at least during sapropel S1 (De Lange et al., 2008), and therefore, age constraints from different sites can be used to cross-tune Eastern Mediterranean records. Grant et al. (2012, 2016) transferred the ages of the well-dated Soreq cave speleothem record to eastern Mediterranean Sea core LC21 using common $\delta^{18}\text{O}$ variability in these two records. Core ODP967, taken close to our core 64PE406-E1, has been synchronized to the LC21 record using both Ba (export-productivity proxy) and $\delta^{18}\text{O}$ variability (Rodríguez-Sanz et al., 2017). Hence, to obtain a robust initial age model, our 64PE406-E1 record is cross-correlated to cores LC21 and ODP967 (see Figure 1 for core locations) using common Ba signals.

Here we study a well-preserved sapropel deposited during MIS-5e, recovered close to the Nile delta, to investigate millennial to centennial time scale climate variability in the Mediterranean Sea. The laminated sediments of the sapropel were analyzed using an X-ray fluorescence (XRF) core scanner. These high-resolution time series were subsequently evaluated in the depth and time domains to establish a new internally independent chronology for the sapropel. For this we use “spectral simplicity” (Schiffelbein & Dorman, 1986), which assumes a more or less constant frequency content on a millennial to centennial time scale to establish an independent depth-to-age calibration. Similar methods have also been used by Park and Herbert (1987) and Herbert (1994) to assess the effects of variations in sedimentation rate records of paleoclimatic variability on orbital time scales. After correcting this way for time-depth distortions, the spectral content of the signal is compared to known frequencies of climate variability. Ultimately, this is used to study in detail the sedimentation in the Nile delta and to study centennial to millennial climate signals in the Mediterranean Sea during the Eemian.

2. Material and Methods

2.1. Sediment Material

Core 64PE406-E1 (33 18.14898°N, 33 23.71998°E, water depth 1,760 m) was collected during the Netherlands Earth System Science Center research cruise in the Eastern Mediterranean Sea conducted with R/V Pelagia in January 2016 (Figure 1). This 9.2-m-long piston core shows an alternation of brown/gray clays with black laminated sapropel sediments. We observe at least four sapropels, which we relate to S1, S3, S4, and S5, at

following depth intervals: S1 is partially present in the top of the piston core and complete in an accompanying multicore; S3 (1.7–2.0 m), S4 (2.5–2.8 m), and S5 (3.3–3.7 m).

2.2. XRF Measurements

The core was analyzed for its geochemical composition using an XRF core scanner (Avaatech) at the Royal Netherlands Institute for Sea Research (NIOZ) in The Netherlands. We used three different voltage settings (10, 30, and 50 kV) to measure all relevant elements from Al to Ba (Richter et al., 2006), and we specifically focus on Ti, Br, Rb, Mo, Mn, and Ba for this study. First, the entire core was scanned at a 1-cm resolution on the “work half” core section (results shown in Figure 3). Second, the interval surrounding sapropel S5 was XRF scanned at a higher 1-mm resolution, again on the “work half” core section (figure 2). Lastly, we measured sapropel S5 in an even higher 400- μm resolution on the “reference half” core section (Figure 4). As the signal-to-noise ratios for the XRF intensities of the elements change with the used resolutions, we assessed the signal-to-noise per element per resolution in order to end up with the highest resolution proxy signal with acceptable signal-to-noise ratio as possible. These tests showed robust signal-to-noise ratios for Ti, Br, Rb, Mo, Mn, and Ba at centimeter and millimeter resolutions, whereas signal-to-noise ratios at 400- μm were sufficient for Br, Rb, Mo, and Ba. The XRF data for sapropel S5 of all presented elements at all measured resolutions is available in the supporting information.

Element ratios, rather than individual elements, are used to prevent closed-sum effects, and log ratios are favored because of asymmetry in normal ratios (Weltje et al., 2015; Weltje & Tjallingii, 2008). Although Al is generally used in geochemical studies for normalization, for XRF core scanning often other elements are used (mainly Ti) as the effect of water absorption is relatively large for a light element as Al (Weltje & Tjallingii, 2008; Hennekam and De Lange., 2012). As the signal-to-noise ratio for Ti was insufficient at the highest (400- μm) resolution, we also used Rb as an element for detrital normalization, which has previously been reported as a good alternative for Mediterranean Sea sediments (Thomson et al., 2006).

2.3. Statistical Approach

When correlating two element-to-element ratios, such as Br/Ti and Ba/Ti, with the same independent variable, correlation may be spurious (Pearson, 1897; Simon, 1954). Pearson (1897) already wrote that such spurious correlations can be recognized by varying the numerator/denominator randomly. Hence, we performed Monte Carlo simulations on the XRF data sets to validate the significance of correlations. Specifically, the XRF data of the numerator variable (e.g., exemplified by Ba in Figure 5) was replaced by a pseudo random variable, having the same statistical distribution and relative range of values as the replaced variable over the selected interval. We subsequently calculated correlation between this pseudo random ratio (random/Ti) and the second element ratio (e.g., exemplified for Mo/Ti in Figure 5). The here used Monte Carlo simulation applied 10^4 draws. From this, an artificial distribution was obtained, showing the correlation based on the spurious correlation only (blue bars in Figures 5C and 5F), representing noise in the numerator only. When the actual correlation (red lines in Figures 5C and 5F) is much higher than the simulated correlations, this confirms statistical significance of the correlation between the actual ratios.

2.4. Frequency Analyses

Time series of the XRF proxy records were analyzed in the time-frequency domain using wavelet transforms (Kirby & Swain, 2013; Torrence & Compo, 1998). Like a windowed Fourier analyses, it uses multiple Fourier transforms to calculate the spectral content of a signal but without the limitation of a uniform time window. A Morlet wavelet with 500 scales and zero padding was used, which is suitable for studying oscillatory signals (Grossmann & Morlet, 1984). In order to focus on sub-Milankovitch cycles, we first removed the offset and trend by subtracting a fitted third-order polynomial, before the actual wavelet analyses. Applying a filter to remove frequency content in which we are not interested would be superfluous, as for each scale of the wavelet the signal is already bandpass filtered at the appropriate frequencies. In a Morlet, a sine curve is multiplied with a Gaussian, with the central wave number setting the width of the Gaussian relative to the frequency. Hence, a higher central wave number increases the width of the sampled interval. Various central wave numbers in the range of 6–12 were used, covering a range of trade-offs between time and frequency resolution (Kirby & Swain, 2013). When higher-frequency resolution is required, a larger central wave number is used, up to 12. For shorter signals however, a low central wave number increases bandwidth, allowing the detection of lower frequencies (Kirby & Swain, 2013). Additionally, a low central wave number increases

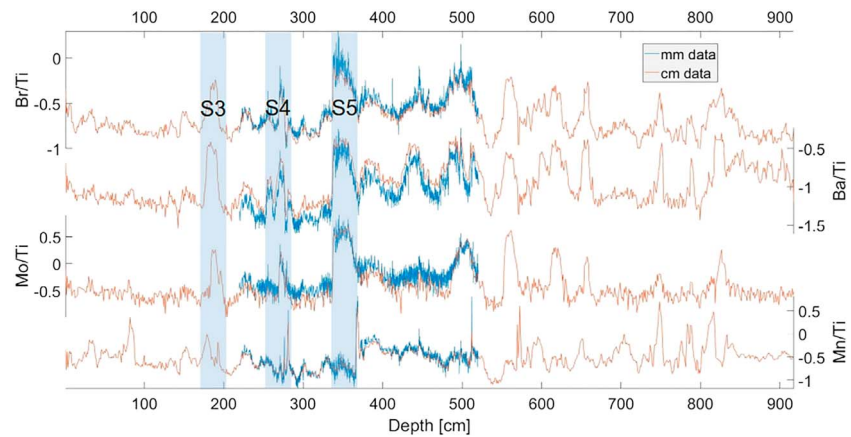


Figure 2. An overview of the centimeter- and millimeter-resolution XRF data of core 64PE406-E1. The blue lines show the millimeter resolution data of each element, and the orange lines the centimeter-resolution data. Various sapropels can be identified; the approximate locations of sapropels S3, S4, and S5 are indicated by the light gray boxes.

time resolution. An integral over the time axis of the wavelet transform was used to calculate a global wavelet. Similar to a frequency power spectrum, a global wavelet shows dominant frequencies and their relative power. When calculating global wavelets, power outside the cone of influence or above the Nyquist frequency is excluded. The Nyquist frequency was calculated by combining our highest XRF resolution of 400 μm with the first-order age model (see below), resulting in a typical Nyquist period of 12–60 years. As these frequency analyses require a constant sampling interval, the XRF data were resampled at an interval of 4 years, prior to analysis, which is shorter than the shortest time interval between two measurement points in any of the age models used (see below), thereby preventing aliasing.

2.5. Age Model and Time-Depth Distortion Removal

The sapropel periods are well expressed through the Ba/Al (or in this case Ba/Ti and/or Ba/Rb) ratio, which approximates the original total organic carbon concentrations (van Santvoort et al., 1996, 1997; De Lange et al., 2008). We transformed the age model of core LC21 (Aegean Sea, Grant et al., 2012, 2016), which was aligned to the excellently dated Soreq cave record, to our 64PE406-E1 core (see Introduction) by tuning the sedimentary Ba/Ti variability (Figure 3). Moreover, we verify this cross-correlation of Ba signals by also comparison of our record to nearby core ODP967, which was also aligned to LC21 using Ba and $\delta^{18}\text{O}$ variability (Rodríguez-Sanz et al., 2017). Variability observed in the Ba/Ti record of core 64PE406-E1 and the Ba intensities of core LC21 and Ba/Ti of core ODP967 are very similar (see Figure 3). Hence, we use the same

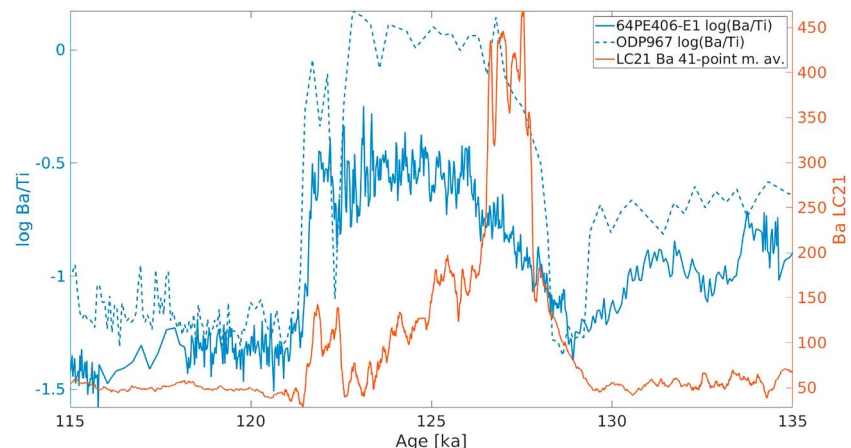


Figure 3. The element log ratios of Ba/Ti sapropel S5 is shown in blue (left axis), compared to the ODP967 Ba/Ti data (also left axis) and the LC21 Ba data.

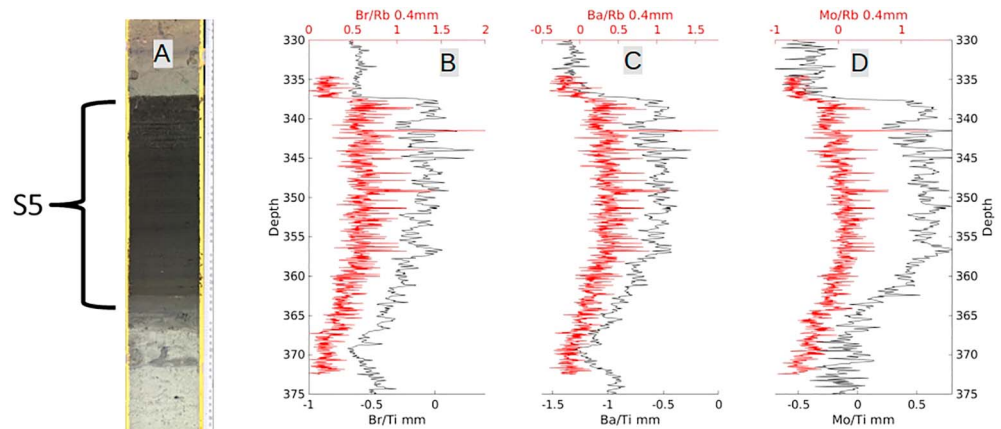


Figure 4. Panel A shows a line scan image of the core interval containing S5, which contains dark organic-rich sediment. Panels B–D show the corresponding graphs of the element log ratios of Br/Ti, Ba/Ti, and Mo/Ti versus depth, respectively, showing an increase in all element ratios during the sapropel.

sapropel S5 boundaries as found by Grant et al. (2016) at 121.5–128.3 kyr BP to constrain our initial age model, which we subsequently improve by removal of time-depth distortions (see below). Note that this approach would not be suitable outside of sapropels, due to a lack of a clear signal.

To study multicentennial variability within S5, we assessed whether the sedimentation rate remains constant throughout the sapropel using a time-frequency analyses. Time-depth distortions are removed by assuming constant frequency content, thereby correcting for sedimentation rate changes within the sapropel. We here follow the same reasoning proposed by Herbert (1994) to remove time-depth distortions for orbital time scales. Time-depth distortions were removed by assuming a constant frequency content on the millennial to centennial time scale by correcting for sedimentation rate changes within the sapropel. To this end, we added pointers to the initial age model at those depths where the frequency content appeared not constant. These pointers were subsequently moved in both time and depth to achieve a more constant frequency content.

3. Results

The centimeter- and millimeter-resolution XRF measurements show good correlations between all ratios (Figure 2). The 0.4-mm-resolution data show much higher-frequency variability, but the same trend as the millimeter-resolution data, with no difference between data normalized to Ti or Rb (Figure 4).

In the sapropel Ba/Ti, Mo/Ti and Br/Ti element ratios are elevated relative to presapropel and postsapropel values. In the XRF data millimeter-scale variability is observed, corresponding to multicentennial time scales (Figure 4). The three element log ratios shown in Figure 4 covariate, even on this millimeter scale. To validate whether this correlation is significant and not spurious, a Monte Carlo simulation has been performed, which randomly varies the numerator of the ratio (Figure 5; see also section 2.3). The correlation between Ba/Ti and Mo/Ti in S5 (see Figure 5) is significant ($R^2 = 0.894$ and $p < 10^{-4}$), while outside the sapropel, we find no correlation ($R^2 < 10^{-2}$ and $p = 0.4859$). This indicates that the data in the sapropel can be used for further analyses of multicentennial climate variability, while the variability outside the sapropel behaves as noise. The wavelet transformation shows the frequency content in the time domain, based on our initial age model (Figure 6a). Although the global wavelet shows distinct frequency peaks, the variability relative to the mean value is very low, as shown in Figure 6c. This relatively low contrast is in line with the drifting frequencies observed in the wavelet transform in Figure 6a. The wavelet transform shows several frequency peaks, which seem to drift over time. At 127 kyr BP, a sudden shift in frequency can be seen in the 400- to 600-year period band (Figure 6a), with the main peak jumping from about 500 to 380 years. From 127–123 ka, the spectral peak in this band slowly appears to increase again to a period of approximately 600 years. After 123 ka, the pattern does not allow to unequivocally distinguish between the different spectral peaks.

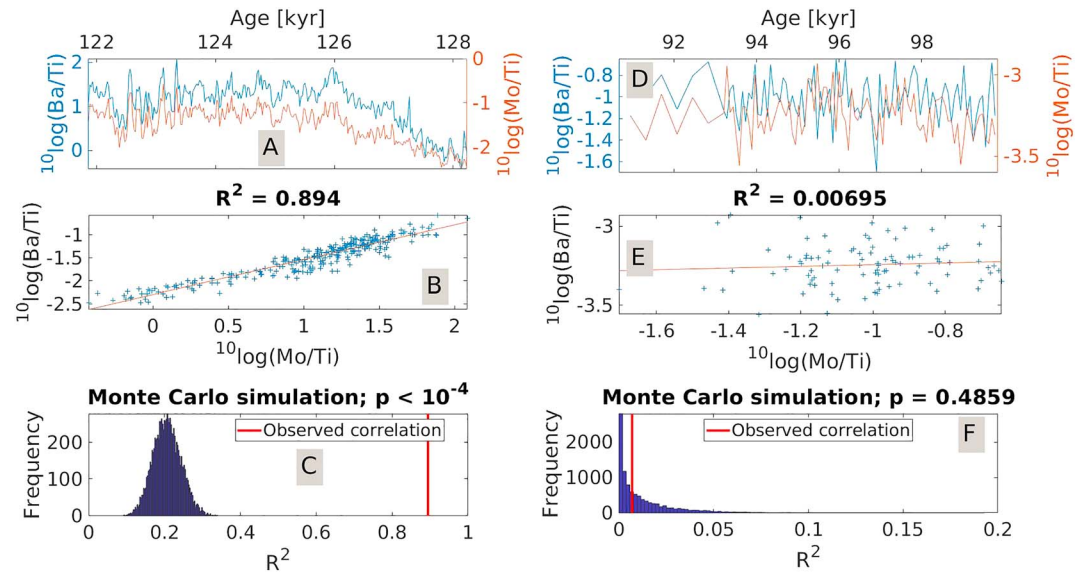


Figure 5. (A, D) A zoom in over the selected interval. (B, E) A correlation plot of these element ratios over the selection interval. (C, F) The results of a Monte Carlo simulation, performed on the selection interval. The distribution (in blue) is the correlation between the two ratios, if Mo, one of the two dependent variables, is replaced by a pseudo random variable, with the same distribution as Mo. The p value indicates the likelihood that a random draw has a better correlation with the second ratio than the measured data, the null hypothesis.

4. Discussion

4.1. Elemental Ratios in Sapropel S5

Even at the highest-frequency variability is found to correlate significantly between the studied element ratios in sapropel S5 (see Figure 5). We can, therefore, use these XRF records to investigate multicentennial

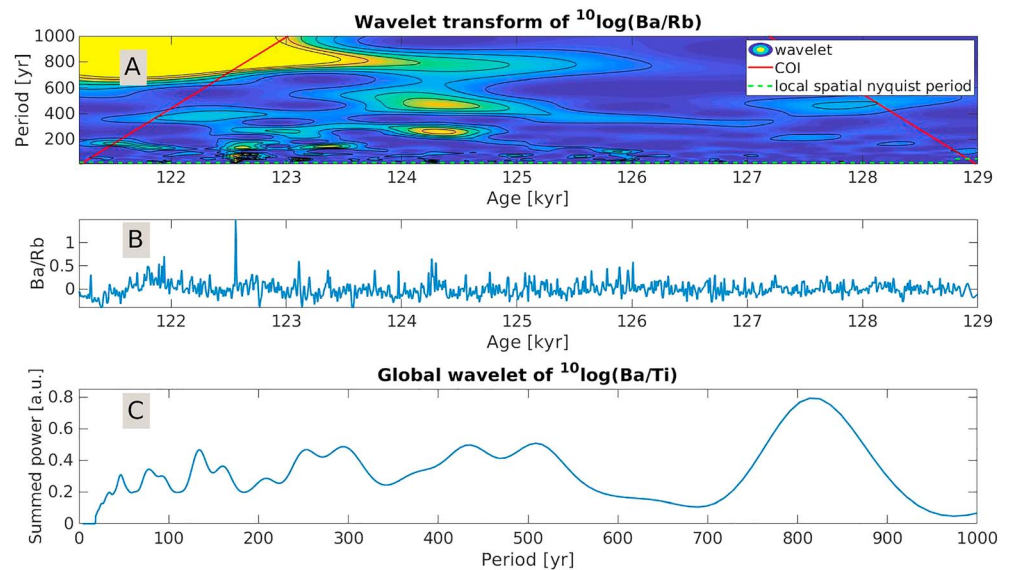


Figure 6. (A) The wavelet transform of the element log ratio of Ba/Rb with a central wave number of 8, when assuming a constant sedimentation rate in sapropel S5. Several frequency components can be observed in the multicentennial band, although the frequencies are not constant. The dashed green line indicates the local spatial Nyquist period, corresponding to the minimal observable period when time-depth distortions are present (Herbert, 1994). The solid red line indicates the cone of influence (COI) of the wavelet transform. (B) The analyzed signal: the element log ratio of Ba/Rb from which the dominant precession signal was removed (see section 2). (C) The integrated power of the wavelet transform over the time axis, a global wavelet. The global wavelet represents a frequency power spectrum.

climate variability within sapropel S5. Normalizing the XRF measurements to Ti may in some settings result in an influence of aeolian dust on the signal, as Saharan dust is enriched in Ti (Lourens et al., 2001). However, we also normalize to Rb, which similarly to Al, is related to the fluvial aluminosilicate component (Thomson et al., 2006). As we find no notable difference between the element/Ti and element/Rb ratios, we conclude that any influence of aeolian dust is very small. Ba/Ti is regarded an indicator of paleo-productivity (e.g., Bishop, 1988; Dymond et al., 1992), while Br/Ti correlates well with marine organic carbon in the Mediterranean Sea (Ziegler et al., 2008). Mo/Ti is a proxy for bottom water anoxia (e.g., Scott & Lyons, 2012; Tribouillard et al., 2006). Nile outflow provides nutrients and fresh water, which is widely assumed to mechanistically underlie sapropel formation (Rohling et al., 2015, and references therein). Moreover, nutricline rise into the lower photic zone (Rohling & Gieskes, 1989) and enhanced regeneration of phosphorus (Slomp et al., 2002) due to anoxic bottom water might have played a major role in the productivity increase during sapropels as well. Consequently, paleo-productivity, sediment organic carbon concentrations, and anoxia are probably all interrelated and controlled by monsoon intensity variability, linked through the River Nile (De Lange et al., 2008; Hennekam et al., 2014; Rohling et al., 2015). In contrast to Mo, Mn precipitates as MnO_2 within the sediment when the bottom waters get oxygenated. Pore-water Mn^{2+} , formed during sapropel formation, diffuses upward and reacts with O_2 , diffusing downward from the oxygen-rich bottom waters, forming Mn oxides. Peak concentrations in Mn can hence be used to indicate burn down (Van Santvoort et al., 1996). Consequently, when a peak in Mn/Ti is found within a sapropel, this indicates that burn down proceeded into the sapropel. Such a Mn/Ti peak is observed within sapropel S3 (see Figure 2) but absent from the top of sapropel S5. This implies that burn down did not appreciably affect the record of S5. Sapropel S5 is hence preserved completely and well suited to assess multicentennial variability in trace elements and fine tuning of the record based on this variability.

4.2. Productivity and Ventilation During Sapropel S5

The covariance of Ba/Rb, Mo/Rb, and Br/Rb during sapropel S5 on multicentennial time scales suggests that the processes causing the fluctuations in these element ratios are also linked. A link between productivity and sediment anoxia has been shown before in the Nile delta region for sapropel S1, also on centennial time scales (Hennekam et al., 2014; Jilbert et al., 2010). These factors are either linked directly (i.e., higher productivity increases oxygen draw down) or indirectly, both reflecting changes in the primary drivers (i.e., Nile outflow is affecting stratification and productivity). Even though these drivers are indistinguishable, the correlation between Ba/Rb and Mo/Rb suggests that surface water productivity and sediment anoxia are coupled in time and through time at the core site. The sapropel S5 record of core LC21 shows an interruption estimated at ~122 ka (Rohling et al., 2006, 2015, and further references therein), which we do not find, as exemplified by our Mo/Ti record. Core LC21 was recovered from the Aegean Sea, closer to a deep water formation site than core 64PE406-E1, potentially making the sediment at the site of core LC21 more sensitive to perturbations. Furthermore, core LC21 is shallower (at 1,520-m depth) and therefore more susceptible to record reventilation events. Still, our data do not allow fully excluding such a weakening in core 64PE406-E1, as the drop in the Ba/Ti record does hint at a period with slightly lower productivity values toward the end of the record, with concurrently also a dip in Mo/Ti, which thus suggests less reducing conditions.

By aligning our Ba/Ti record with the LC21 Ba record, we assume synchronous productivity variability throughout the Mediterranean Sea, within uncertainties. Marino et al. (2007) suggest that anoxia at the site of LC21 developed ~100–300 years earlier when compared to an open Mediterranean Sea core (OPD971). However, within age model uncertainties at the sapropel boundaries (2 kyr), the influence of this type of nonsynchronous developments are relatively insignificant, as this would imply an additional uncertainty of approximately 3% in the total length of the sapropel. Moreover, we aligned our record using the barium record, which is not assuming a synchronous development of anoxia but productivity during the same period. While it needs to be seen that such developments are absolutely synchronous, we conclude that there is no indication that this is an issue for our analysis.

4.3. Multicentennial Paleo-Environmental Variability During Sapropel S5 and Removal of the Time-Depth Distortion

The first-order age model (Figure 3 and section 4) assumes a constant sedimentation rate for sapropel S5, as no radiometric dates are available within sapropel S5 (and there is no evidence that intrasapropel variability occurs time-synchronous basin wide). Hence, there is need for an independent age model that removes time-

depth distortions in the core at a sufficiently high resolution. The first-order age model showed several significant spectral peaks in the power spectrum, and the wavelet transform shows that these frequencies appear to vary through depth (Figure 6). Hence, we subsequently tuned the age model as to achieve constant frequencies throughout the sapropel, allowing deviations from a constant sedimentation rate. The minimum change in sedimentation rate needed to obtain constant frequencies corresponds to a maximum offset (in the middle of the sapropel) of 1.5 kyr from the original linear age model, which is within the uncertainty of the sapropel boundaries (Grant et al., 2016 report uncertainties [2σ] of 2.0 ± 0.9 kyr for the 40- to 150-ka BP interval). The new age model results from the hypothesis that a significant, constant frequency spectrum exists in the time domain. Still, we here refrain from speculating on a specific driving mechanism, or linkages to specific frequencies present in the signal, but rather present the methods as such to allow using the internal changes in sedimentation rate, irrespective of the frequencies present.

By adding a single pointer to the age model within the sapropel, a low frequency peak of around 650 years becomes constant throughout the sapropel. However, with this age model, higher frequency components are not constant. By adding additional pointers, all observed spectral components can be made much more stable during sapropel S5 (Figure 7a). A spline interpolation is used between these pointers, to prevent abrupt changes in sedimentation rate. The amplitude of the spectral peaks in the global wavelet is a measure for the stability of the frequency components: When the frequencies are less constant through time, more power will accumulate between peaks. The global wavelet of the first age model (Figure 6c) shows much less contrast between the peaks compared to the global wavelet of the tuned age model (Figure 7). This suggests that the tuned age model provides an appreciable improvement, when assuming spectral simplicity.

When a pointer in the tuned age model is shifted by more than 100 years, the frequency content becomes significantly less constant. This indicates that tuning errors are at most 100 years and do not significantly contribute to the overall error in the frequency content. The uncertainty in the time domain is related to the uncertainties of the dating of the core LC21 and, hence, are in the order of 2 ± 0.9 kyr over sapropel S5 (Grant et al., 2016). Each of the frequency components therefore also has an uncertainty proportional to the uncertainty in sapropel duration.

Possible forcing mechanisms for multicentennial climate variability include, but are not restricted to, solar variability, North Atlantic Oscillation, and the El Niño–Southern Oscillation. Solar variability is characterized by distinct spectral components, at least during the Holocene (i.e., Dykoski et al., 2005; Wang et al., 2005). The North Atlantic Oscillation has been considered as a driving mechanism but does not contain distinct frequency components and behaves as blue noise (i.e., noise with reduced high frequency components; Cook et al., 2002). The El Niño–Southern Oscillation may also have affected sapropel formation through monsoon and in particular Nile outflow variability, since frequencies similar to those found in El Niño–Southern Oscillation records are recognized in the Nile high water anomaly record (Kondrashov et al., 2005). However, these frequencies are much higher than the Nyquist frequency of the sapropel S5 XRF record and can therefore not be detected. To validate potential impact of solar variability as a driving mechanism, we compare its frequency content to that of the sapropel S5 XRF record (section 5.4) We indeed observe an overall similar frequency content, although this does not necessarily imply causality. For instance, throughout the Holocene, it has been suggested that solar forcing affects the El Niño–Southern Oscillation (Marchitto et al., 2010), which in turn may affect the African monsoon.

4.4. High-Frequency Climate Signals in the Sapropel S5

The tuned age model removes time-depth distortion from the signal and therefore allows us to compare the spectral content of intrasapropel variability to other records. An important mechanism proposed for the variability within the most recent sapropel (S1) is solar activity (Hennekam et al., 2014; Jilbert et al., 2010). Rohling et al. (2002) already proposed solar activity as a driver for variability within sapropel S5, although no clear mechanism was given at that time. The ~88-year periodicity found here (in Ba/Rb) was also observed before in both a Nile high water anomaly record (Ruzmaikin et al., 2006) and total solar irradiance (TSI)/sunspot records (Steinhilber et al., 2012 and the Sunspot Index and Long-term Solar Observations (SILSO), respectively). Therefore, it seems that solar activity affects monsoon intensity, which in turn affects Nile discharge, also when overall Nile discharge is much higher. Even when increased Nile discharge due to precession variability causes an overall increase in productivity and oxygen drawdown in the Mediterranean, superimposed changes are still observed. Furthermore, Duan et al. (2014)

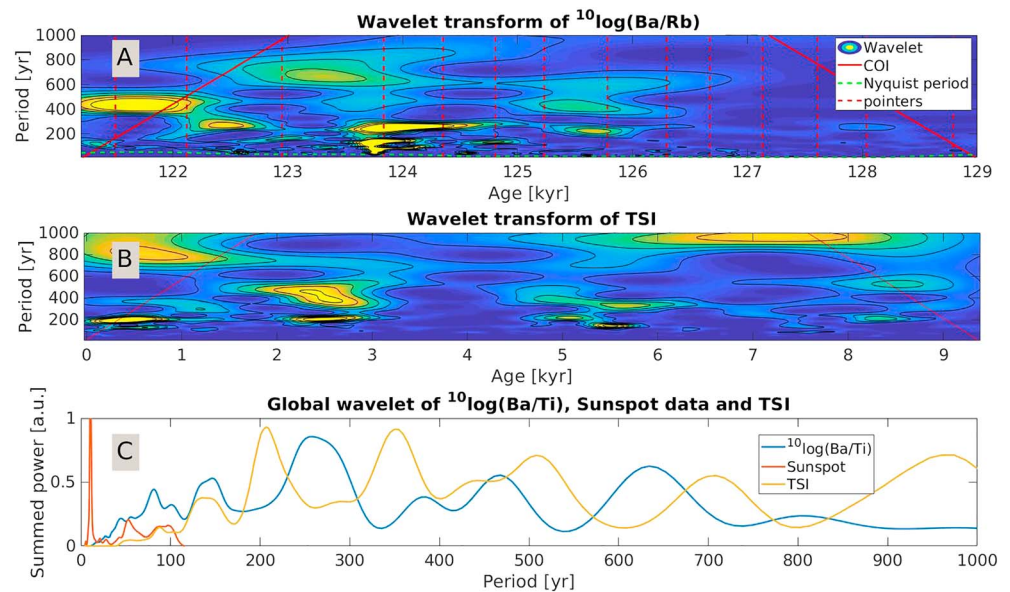


Figure 7. (A) The wavelet transform of the element log ratio of Ba/Rb with the tuned age model, with a central wave number of 8. The dashed green line indicates the local spatial Nyquist period, corresponding to the minimal observable period when time-depth distortions are present (Herbert, 1994). The solid red line indicates the cone of influence (COI) of the wavelet transform. (B) A wavelet transform of the total solar irradiance (TSI), using the same wavelet settings. Although the signals originate from different time intervals, their frequency-time behavior has similarities as shown in the wavelet transforms. (C) The Br/Rb global wavelet using the tuned age model, compared to global wavelets of TSI (Steinhilber et al., 2012) and sunspot data (SILSO). Most peaks of the Br/Rb global wavelet have corresponding peaks in either the sunspot data or the TSI data. A central wave number of 12 was used for the TSI and XRF data (providing more frequency resolution), while a central wave number of 6 is used for the sunspot data.

showed how the Asian Monsoon activity is modulated by changes in solar activity, with monsoon variability most likely forced by the cosmic ray flux and associated changes in cloud cover. In addition, reduced solar output is thought to weaken the thermal contrast between ocean and continent or between hemispheres, reducing monsoon circulation and associated rainfall (Wang et al., 2017; Yan et al., 2015). The Nile river discharge may also be affected by Atlantic Meridional Overturning Circulation (AMOC) slowdown or shutdown, like during the last glacial stadials and Heinrich events (Broccoli et al., 2006; Wang et al., 2005), as millennial-scale AMOC variability has been found during MIS 5e (e.g., Oppo et al., 2001). However, clear spectral peaks in the frequency band relevant to this study (periods of 70–1,000 years) have not been reported in these records. We therefore conclude that while AMOC variability may have affected Nile outflow during sapropel S5, it cannot explain the variability observed in this study.

Several dominant frequencies have been observed in the reconstructed total solar irradiance over the past 9 kyr, such as 210 (the Suess cycle), 350 and 710 years (Steinhilber et al., 2012). However, similar solar cycles have not yet been identified as far back in time as sapropel S5. In order to explore solar cycles as a forcing mechanism for intrasapropel variability, we compare the frequency content of our XRF data to that of the TSI (Steinhilber et al., 2012) and the more recent sunspot number data (SILSO, which has yearly resolution). The same wavelet analysis has been performed on all data sets. A direct comparison between the wavelet transforms of Ba/Rb and TSI (Figures 7A and 7B) shows similar periodicities at high frequencies and similar patterns in relative intensity at lower frequencies. The sunspot data cover the last 300 years and can therefore only be used for periods shorter than 200 years. The TSI has a length of 9,000 years, comparable to the duration of sapropel S5, with a sampling interval of 22 years. The TSI can hence be used for periods longer than 44 years. The intensity of the dominant frequencies in the TSI data vary over time (Steinhilber et al., 2012) but not in frequency. Most frequencies correspond to TSI and sunspot periodicities within error (approximately 20%); however, we refrain from adjusting the age model based on this, as also other causes for high-frequency variability exist. The similarity of the frequencies observed, as well as the stability of the frequencies observed, supports our initial assumption of constant frequency components. Note that

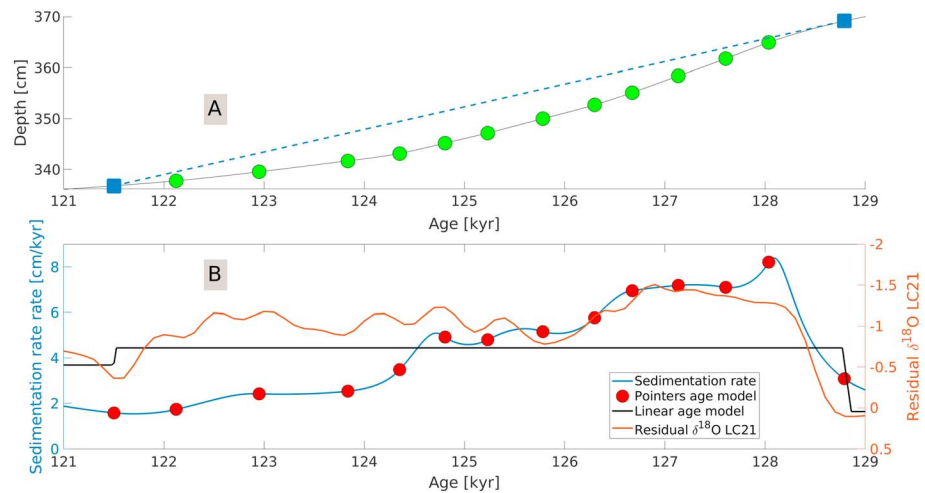


Figure 8. (A) The final age-depth relation (solid line, the dots represent the pointers), compared to the linear age model (dashed line). (B) The sedimentation rate in sapropel S5 (~129–121 ka) resulting from the tuned age model (blue line with the red dots), with the sedimentation rate from the untuned, linear age model for comparison (black line). Note the higher sedimentation rate at the start of the sapropel in the tuned age model. Due to the high number of control points in S5, a spline interpolation is more appropriate than a linear interpolation, which would result in abrupt steps in sedimentation rate at each pointer. Consequently, the sedimentation rate changes smoothly between the pointers. The orange line shows the residual $\delta^{18}\text{O}$, derived from core LC21 (Grant et al., 2012).

shorter quasi-cycles, such as those with ~11 (sunspot or Schwabe cycles) and ~22 (Hale cycles) year periodicities cannot be observed in our record, as the temporal resolution is insufficient.

Relative power of the spectral peaks in the XRF, TSI and sunspot data differs significantly, which is expected since relative power is not constant through time in the TSI data either (Figures 7B and 7C). Moreover, it is highly unlikely that processes affecting the proxy records in the different frequency domains are linearly related to the driving forces. More importantly, the patterns of the intensity of the different frequencies in the wavelet plot (Figures 7A and 7B) are similar. We hence conclude that the time-frequency spectra of the records support the hypothesis that intra-sapropel S5 variability is related to solar cycles.

As consequence of the internal tuning of the age model, with the aim to remove time-depth distortions, sedimentation rates within the sapropel is constrained (Figure 8). The derived sedimentation rates closely resemble the monsoon intensity reconstruction as derived from residual LC21 $\delta^{18}\text{O}$ (Grant et al., 2016). This record shows a steep increase toward maximum monsoon intensity, after which gradual decline of monsoon strength is observed. A link between climate and sedimentation rate has been proposed by Schiffelbein and Dorman (1986), who used a very similar criterion, “spectral simplicity.” Still the pattern deviates from that found in the Nile delta for sapropel S1 (Hennekam et al., 2015). This difference may be due to the fact that the record used here is from a more distal location, whereas the Nile delta record is affected directly by the local sedimentary system, where magnitude response and phase response may be very different. Sea level might be an important factor to explain this difference, as it can have a large effect on sedimentation, especially during sapropel S1. Whereas a sea level change would decrease the local sedimentation rate (i.e., the site becomes more distal during sea level rise) during S1, sedimentation rate would go up during the early stage of S5 (monsoon only) as at the onset of sapropel S5 the peak in monsoon intensity was much higher than during S1 (Grant et al., 2016; Rohling et al., 2004).

5. Conclusions

We propose a novel method to remove time-depth distortions on a multicentennial scale, by assuming so-called spectral simplicity, and apply this method to sediments from the Eastern Mediterranean Sea that record the anoxia event (sapropel S5) during the Eemian. A small shift in tuning ages (within age model uncertainty), and thus sedimentation rate, is sufficient to stabilize all spectral components during sapropel S5. This allows to assess the multicentennial climate variability in our proxy records for productivity and

anoxia, related to sapropel S5 formation, with more certainty. The resulting signal showed similarity to several records of solar activity from the Holocene, both in frequency and amplitude variability. Hence, we conclude that intrasapropel variability, at least during sapropel S5, seems to be linked to solar variability through Nile outflow. Moreover, this suggests that multicentennial climate variability that affected sapropel formation during the Holocene and the “warmer-than-preindustrial” Eemian behaved in a similar way.

Our age model, which removes time-depth distortions, also allows us to study the sedimentation rate in unprecedented detail. The early phase of sapropel S5 was characterized by an intensified Nile outflow. The sedimentation rates during this phase, calculated from the age model are found to be higher. After this initial peak, the derived sedimentation rate gradually decreases again, similar to the reduction in Nile discharge that has been reconstructed. Hence, the monsoon intensity and sedimentation rate at the core location were probably linked during sapropel S5.

Acknowledgments

The authors would like to thank Rineke Gielens for helping with the XRF measurements. We acknowledge chief Scientist Marcel van der Meer and the crew of the R/V Pelagia for their extensive help during the first NESSC Mediterranean cruise. We would like to thank the editor (professor Stephen Barker), reviewer Gianluca Marino, and another anonymous reviewer for their constructive comments and recommendations. This work was carried out under the program of the Netherlands Earth System Science Centre (NESSC), financially supported by the Ministry of Education, Culture and Science (OCW; Grant 024.002.001) This research is made possible by financial support to the SCANALOGUE-project (ALWOP.2015.113) by the Netherlands Organization for Scientific Research (NWO) and The Netherlands Research Centre for Integrated Solid Earth Science (ISES 2017-UU-23). The published data are archived in the PANGAEA data repository (<https://doi.pangaea.de/10.1594/PANGAEA.899596>).

References

- Altabet, M. A., Higginson, M. J., & Murray, D. W. (2002). The effect of millennial-scale changes in Arabian Sea denitrification on atmospheric CO₂. *Nature*, *415*(6868), 159.
- Barker, S., Knorr, G., Edwards, R. L., Parrenin, F., Putnam, A. E., Skinner, L. C., et al. (2011). 800,000 years of abrupt climate variability. *Science*, *334*(6054), 347–351. <https://doi.org/10.1126/science.1203580>
- Bishop, J. K. B. (1988). The barite-opal-organic carbon association in oceanic particulate matter. *Nature*, *332*, 341–343.
- Blaga, C. I., Reichert, G. J., Lotter, A. F., Anselmetti, F. S., & Sinninghe Damsté, J. S. (2013). A TEX86 lake record suggests simultaneous shifts in temperature in Central Europe and Greenland during the last deglaciation. *Geophysical Research Letters*, *40*, 948–953. <https://doi.org/10.1002/grl.50181>
- Bond, G., Broecker, W., Johnsen, S., McManus, J., Labeyrie, L., Jouzel, J., & Bonani, G. (1993). Correlations between climate records from North Atlantic sediments and Greenland ice. *Nature*, *365*(6442), 143.
- Bond, G., Showers, W., Cheseby, M., Lott, R., Almasi, P., deMenocal, P., et al. (1997). A pervasive millennial-scale cycle in North Atlantic Holocene and glacial climates. *Science*, *278*(5341), 1257–1266.
- Broccoli, A. J., Dahl, K. A., & Stouffer, R. J. (2006). Response of the ITCZ to Northern Hemisphere cooling. *Geophysical Research Letters*, *33*, L01702. <https://doi.org/10.1029/2005GL024546>
- Capron, E., Govin, A., Feng, R., Otto-Bliessner, B. L., & Wolff, E. W. (2017). Critical evaluation of climate syntheses to benchmark CMIP6/PMIP4 127 ka Last Interglacial simulations in the high-latitude regions. *Quaternary Science Reviews*, *168*, 137–150.
- Cook, E. R., D'Arrigo, R. D., & Mann, M. E. (2002). A well-verified, multiproxy reconstruction of the winter North Atlantic Oscillation index since AD 1400. *Journal of Climate*, *15*(13), 1754–1764.
- Cramp, A., & O'Sullivan, G. (1999). Neogene sapropels in the Mediterranean: A review. *Marine Geology*, *153*(1), 11–28.
- Dansgaard, W., Johnsen, S. J., Clausen, H. B., Dahl-Jensen, D., Gundestrup, N. S., Hammer, C. U., et al. (1993). Evidence for general instability of past climate from a 250-kyr ice-core record. *Nature*, *364*(6434), 218–220.
- De Lange, G. J., Thomson, J., Reitz, A., Slomp, C. P., Principato, M. S., Erba, E., & Corselli, C. (2008). Synchronous basin-wide formation and redox-controlled preservation of a Mediterranean sapropel. *Nature Geoscience*, *1*(9), 606–610.
- Duan, F., Wang, Y., Shen, C. C., Wang, Y., Cheng, H., Wu, C. C., et al. (2014). Evidence for solar cycles in a late Holocene speleothem record from Dongge Cave, China. *Scientific Reports*, *4*, 5159.
- Dykoski, C. A., Edwards, R. L., Cheng, H., Yuan, D., Cai, Y., Zhang, M., et al. (2005). A high-resolution, absolute-dated Holocene and deglacial Asian monsoon record from Dongge Cave, China. *Earth and Planetary Science Letters*, *233*(1–2), 71–86.
- Dymond, J., Suess, E., & Lyle, M. (1992). Barium in deep-sea sediment: A geochemical proxy for paleoproductivity. *Paleoceanography*, *7*(2), 163–181.
- Grant, K. M., Grimm, R., Mikolajewicz, U., Marino, G., Ziegler, M., & Rohling, E. J. (2016). The timing of Mediterranean sapropel deposition relative to insolation, sea-level and African monsoon changes. *Quaternary Science Reviews*, *140*.
- Grant, K. M., Rohling, E. J., Bar-Matthews, M., Ayalon, A., Medina-Elizalde, M., Ramsey, C. B., et al. (2012). Rapid coupling between ice volume and polar temperature over the past 150,000 years. *Nature*, *491*(7426), 744–747.
- Greenland Ice-core Project (GRIP) Members (1993). Climate instability during the last interglacial period recorded in the GRIP ice core. *Nature*, *364*, 203–207.
- Grootes, P. M., Stuiver, M., White, J. W. C., Johnsen, S., & Jouzel, J. (1993). Comparison of oxygen isotope records from the GISP2 and GRIP Greenland ice cores. *Nature*, *366*(6455), 552.
- Grossmann, A., & Morlet, J. (1984). Decomposition of Hardy functions into square integrable wavelets of constant shape. *SIAM Journal on Mathematical Analysis*, *15*(4), 723–736.
- Haug, G. H., Hughen, K. A., Sigman, D. M., Peterson, L. C., & Röhl, U. (2001). Southward migration of the intertropical convergence zone through the Holocene. *Science*, *293*(5533), 1304–1308.
- Heinrich, H. (1988). Origin and consequences of cyclic ice rafting in the northeast Atlantic Ocean during the past 130,000 years. *Quaternary Research*, *29*(2), 142–152.
- Hennekam, R., & De Lange, G. (2012). X-ray fluorescence core scanning of wet marine sediments: Methods to improve quality and reproducibility of high-resolution paleoenvironmental records. *Limnology and Oceanography: Methods*, *10*, 991–1003.
- Hennekam, R., Donders, T. H., Zwiep, K., & de Lange, G. J. (2015). Integral view of Holocene precipitation and vegetation changes in the Nile catchment area as inferred from its delta sediments. *Quaternary Science Reviews*, *130*, 189–199.
- Hennekam, R., Jilbert, T., Schnetger, B., & Lange, G. J. (2014). Solar forcing of Nile discharge and sapropel S1 formation in the early to middle Holocene eastern Mediterranean. *Paleoceanography*, *29*, 343–356. <https://doi.org/10.1002/2013PA002553>
- Herbert, T. D. (1994). Reading orbital signals distorted by sedimentation: Models and examples. In P. L. DeBoer & G. D. Smith (Eds.), *Orbital forcing and cyclic sequences, International Association of Sedimentologist, Special Publications* (Vol. 19, pp. 483–507).
- Hilgen, F. J. (1991). Extension of the astronomically calibrated (polarity) time scale to the Miocene/Pliocene boundary. *Earth and Planetary Science Letters*, *107*(2), 349–368.

- Hoffman, J. S., Clark, P. U., Parnell, A. C., & He, F. (2017). Regional and global sea-surface temperatures during the last interglaciation. *Science*, 355(6322), 276–279.
- Jilbert, T., Reichert, G. J., Mason, P., & de Lange, G. J. (2010). Short-time-scale variability in ventilation and export productivity during the formation of Mediterranean sapropel S1. *Paleoceanography*, 25, PA4232. <https://doi.org/10.1029/2010PA001955>
- Kemp, A. E., Pearce, R. B., Koizumi, I., Pike, J., & Rance, S. J. (1999). The role of mat-forming diatoms in the formation of Mediterranean sapropels. *Nature*, 398(6722), 57.
- Kirby, J. F., & Swain, C. J. (2013). Power spectral estimates using two-dimensional Morlet-fan wavelets with emphasis on the long wavelengths: Jackknife errors, bandwidth resolution and orthogonality properties. *Geophysical Journal International*, ggt103.
- Kondrashov, D., Feliks, Y., & Ghil, M. (2005). Oscillatory modes of extended Nile River records (AD 622–1922). *Geophysical Research Letters*, 32, L10702. <https://doi.org/10.1029/2004GL022156>
- Krom, M. D., Stanley, J. D., Cliff, R. A., & Woodward, J. C. (2002). Nile River sediment fluctuations over the past 7000 yr and their key role in sapropel development. *Geology*, 30(1), 71–74.
- Lourens, L. J., Antonarakou, A., Hilgen, F. J., Van Hoof, A. A. M., Vergnaud-Grazzini, C., & Zachariasse, W. J. (1996). Evaluation of the Plio-Pleistocene astronomical timescale. *Paleoceanography*, 11(4), 391–413.
- Lourens, L. J., Wehausen, R., & Brumsack, H. J. (2001). Geological constraints on tidal dissipation and dynamical ellipticity of the Earth over the past three million years. *Nature*, 409(6823), 1029.
- Marchitto, T. M., Muscheler, R., Ortiz, J. D., Carriquiry, J. D., & van Geen, A. (2010). Dynamical response of the tropical Pacific Ocean to solar forcing during the early Holocene. *Science*, 330(6009), 1378–1381.
- Marino, G., Rohling, E. J., Rijpstra, W. I. C., Sangiorgi, F., Schouten, S., & Damsté, J. S. S. (2007). Aegean Sea as driver of hydrographic and ecological changes in the eastern Mediterranean. *Geology*, 35(8), 675–678.
- NEEM-community-members (2013). Eemian interglacial reconstructed from a Greenland folded ice core. *Nature*, 493(7433), 489.
- Oppo, D. W., Keigwin, L. D., McManus, J. F., & Cullen, J. L. (2001). Persistent suborbital climate variability in marine isotope stage 5 and Termination II. *Paleoceanography*, 16(3), 280–292.
- Oppo, D. W., McManus, J. F., & Cullen, J. L. (2006). Evolution and demise of the Last Interglacial warmth in the subpolar North Atlantic. *Quaternary Science Reviews*, 25(23), 3268–3277.
- Park, J., & Herbert, T. D. (1987). Hunting for paleoclimatic periodicities in a geologic time series with an uncertain time scale. *Journal of Geophysical Research*, 92(B13), 14,027–14,040.
- Pearson, K. (1897). Mathematical contributions to the theory of evolution.—On a form of spurious correlation which may arise when indices are used in the measurement of organs. *Proceedings of the Royal Society of London*, 60(359-367), 489–498.
- Richter, T. O., Van Der Gaast, S., Koster, B., Vaars, A., Gieles, R., De Stijter, H. C., et al. (2006). The Avaatech XRF core scanner: Technical description and applications to NE Atlantic sediments. In R. G. Rothwell (Ed.), *New Techniques in Sediment Core Analysis*, Geological Society Special Publication (pp. 39–50).
- Rodríguez-Sanz, L., Bernasconi, S. M., Marino, G., Heslop, D., Mueller, I. A., Fernandez, A., et al. (2017). Penultimate deglacial warming across the Mediterranean Sea revealed by clumped isotopes in foraminifera. *Scientific Reports*, 7(1), 16572. <https://doi.org/10.1038/s41598-017-16528-6>
- Rohling, E. J., Cane, T. R., Cooke, S., Sprovieri, M., Bouloubassi, I., Emeis, K. C., et al. (2002). African monsoon variability during the previous interglacial maximum. *Earth and Planetary Science Letters*, 202(1), 61–75.
- Rohling, E. J., & Gieskes, W. W. C. (1989). Late Quaternary changes in Mediterranean intermediate water density and formation rate. *Paleoceanography*, 4(5), 531–545.
- Rohling, E. J., Hopmans, E. C., & Sinninghe Damsté, J. S. (2006). Water column dynamics during the last interglacial anoxic event in the Mediterranean (sapropel S5). *Paleoceanography*, 21, PA2018. <https://doi.org/10.1029/2005PA001237>
- Rohling, E. J., Marino, G., & Grant, K. M. (2015). Mediterranean climate and oceanography, and the periodic development of anoxic events (sapropels). *Earth-Science Reviews*, 143, 62–97.
- Rohling, E. J., Sprovieri, M., Cane, T., Casford, J. S. L., Cooke, S., Bouloubassi, I., et al. (2004). Reconstructing past planktic foraminiferal habitats using stable isotope data: A case history for Mediterranean sapropel S5. *Marine Micropaleontology*, 50(1), 89–123.
- Rosignol-Strick, M. (1985). Mediterranean Quaternary sapropels, an immediate response of the African monsoon to variation of insolation. *Palaeogeography, Palaeoclimatology, Palaeoecology*, 49(3), 237–263.
- Rosignol-Strick, M., Nesteroff, W., Olive, P., & Vergnaud-Grazzini, C. (1982). After the deluge: Mediterranean stagnation and sapropel formation. *Nature*, 295(5845), 105–110.
- Ruzmaikin, A., Feynman, J., & Yung, Y. L. (2006). Is solar variability reflected in the Nile River. *Journal of Geophysical Research*, 111, D21114. <https://doi.org/10.1029/2006JD007462>
- Schiffelbein, P., & Dorman, L. (1986). Spectral effects of time-depth nonlinearities in deep sea sediment records: A demodulation technique for realigning time and depth scales. *Journal of Geophysical Research*, 91(B3), 3821–3835.
- Scott, C., & Lyons, T. W. (2012). Contrasting molybdenum cycling and isotopic properties in euxinic versus non-euxinic sediments and sedimentary rocks: Refining the paleoproxies. *Chemical Geology*, 324–325, 19–27.
- Simon, H. A. (1954). Spurious correlation: A causal interpretation. *Journal of the American Statistical Association*, 49(267), 467–479.
- Slomp, C. P., Thomson, J., & de Lange, G. J. (2002). Enhanced regeneration of phosphorus during formation of the most recent eastern Mediterranean sapropel (S1). *Geochimica et Cosmochimica Acta*, 66(7), 1171–1184.
- Steinhilber, F., Abreu, J. A., Beer, J., Brunner, I., Christl, M., Fischer, H., et al., (2012). 9,400 years of cosmic radiation and solar activity from ice cores and tree rings. *Proceedings of the National Academy of Sciences*, 109(16), 5967–5971.
- SILSO data/image (n.d.). Sunspot data. Royal Observatory of Belgium, Brussels. Retrieved from <http://sidc.be/silso/home>
- Thomson, J., Croudace, I. W., & Rothwell, R. G. (2006). A geochemical application of the ITRAX scanner to a sediment core containing eastern Mediterranean sapropel units. *Geological Society, London, Special Publications*, 267(1), 65–77.
- Torrence, C., & Compo, G. P. (1998). A practical guide to wavelet analysis. *Bulletin of the American Meteorological Society*, 79(1), 61–78. Wavelet software was provided by C. Torrence and G. Compo, and is available at URL: <http://paos.colorado.edu/research/wavelets/>.
- Tribouillard, N., Algeo, T. J., Lyons, T., & Riboulleau, A. (2006). Trace metals as paleoredox and paleoproductivity proxies: An update. *Chemical Geology*, 232, 12–32.
- Tzedakis, P. C., Crucifix, M., Mitsui, T., & Wolff, E. W. (2017). A simple rule to determine which insolation cycles lead to interglacials. *Nature*, 542(7642), 427–432.
- van Santvoort, P. J. M., De Lange, G. J., Thomson, J., Cussen, H., Wilson, T. R. S., Krom, M. D., & Ströhl, K. (1996). Active post-depositional oxidation of the most recent sapropel (S1) in sediments of the eastern Mediterranean Sea. *Geochimica et Cosmochimica Acta*, 60(21), 4007–4024.

- van Santvoort, P. J. M., Lange, G. J., Langereis, C. G., Dekkers, M. J., & Paterne, M. (1997). Geochemical and paleomagnetic evidence for the occurrence of “missing” sapropels in eastern Mediterranean sediments. *Paleoceanography*, *12*(6), 773–786.
- Wang, P. X., Wang, B., Cheng, H., Fasullo, J., Guo, Z., Kiefer, T., & Liu, Z. (2017). The global monsoon across time scales: Mechanisms and outstanding issues. *Earth-Science Reviews*, *174*, 84–121.
- Wang, Y., Cheng, H., Edwards, R. L., He, Y., Kong, X., An, Z., et al. (2005). The Holocene Asian monsoon: Links to solar changes and North Atlantic climate. *Science*, *308*(5723), 854–857.
- Wang, Y. J., Cheng, H., Edwards, R. L., An, Z. S., Wu, J. Y., Shen, C. C., & Dorale, J. A. (2001). A high-resolution absolute-dated late Pleistocene monsoon record from Hulu Cave, China. *Science*, *294*(5550), 2345–2348.
- Weltje, G. J., Bloemsa, M. R., Tjallingii, R., Heslop, D., Röhl, U., & Croudace, I. W. (2015). Prediction of geochemical composition from XRF core scanner data: A new multivariate approach including automatic selection of calibration samples and quantification of uncertainties. In *Micro-XRF Studies of Sediment Cores* (pp. 507–534). Netherlands: Springer.
- Weltje, G. J., & Tjallingii, R. (2008). Calibration of XRF core scanners for quantitative geochemical logging of sediment cores: Theory and application. *Earth and Planetary Science Letters*, *274*(3), 423–438.
- Yan, H., Wei, W., Soon, W., An, Z., Zhou, W., Liu, Z., et al. (2015). Dynamics of the intertropical convergence zone over the western Pacific during the Little Ice Age. *Nature Geoscience*, *8*(4), 315.
- Ziegler, M., Jilbert, T., de Lange, G. J., Lourens, L. J., & Reichert, G. J. (2008). Bromine counts from XRF scanning as an estimate of the marine organic carbon content of sediment cores. *Geochemistry, Geophysics, Geosystems*, *9*, Q05009. <https://doi.org/10.1029/2007GC001932>